JOURNAL OF MAGNETIC RESONANCE 89, 297–309 (1990)

NMR Experiments with a New Double Rotor

Y. WU, B. Q. SUN, AND A. PINES*

Lawrence Berkeley Laboratory and University of California, Berkeley, California, 94720

AND

A. SAMOSON AND E. LIPPMAA

Institute of Chemical Physics and Biophysics, Estonian Academy of Sciences, Tallinn 200 001, Estonia

Received January 25, 1990

We describe a new double-rotor design that achieves an outer-rotor speed of about 1 kHz and an inner-rotor speed of 5 kHz under conditions of double rotation. Mechanical analysis and experimental data are presented illustrating the mechanism and optimal conditions for the double-rotor motion. The performance of this double rotor is demonstrated by double-rotation NMR spectra of ^{23}Na and ^{17}O in some polycrystalline compounds where the static NMR spectra are broadened by dipole–dipole and second-order quadrupole interactions. Spectra obtained by synchronizing the double rotor with radiofrequency pulses are in agreement with computer simulations.

The work of Andrew *et al.* and Lowe (*1*) over 30 years ago to reduce dipole–dipole line broadening by means of magic-angle spinning (MAS) showed that mechanical motion of the sample is a useful approach to resolution enhancement for solid-state NMR. Since then, other types of sample motion have been demonstrated (*2*), most recently the introduction of double rotation (DOR) and dynamic angle spinning (DAS) (*3*).

In the DOR NMR probe (*4*), the sample is contained in a small, fast-spinning inner rotor; this inner rotor is embedded in the body of a large outer rotor which spins at the magic angle $\beta_2 = 54.74°$ with respect to the static magnetic field; the angle β_1 between the spinning axes of the inner and outer rotors is 30.56°. One of the applications of the DOR technique is to narrow the central NMR transition ($\frac{1}{2} \leftrightarrow -\frac{1}{2}$) of half-odd-integer quadrupolar nuclei; the central transition is broadened, among other effects, by anisotropic second-order quadrupole interactions. For example, the static linewidth of the ^{23}Na central transition in polycrystalline sodium oxalate powder, which is about 10 kHz in a 400 MHz (proton) spectrometer, was narrowed by DOR down to 150 Hz without losing information about the isotropic shift.

One of the problems associated with DOR spectra is the large number of sidebands originating from the slowly spinning outer rotor whose angular frequency is consid-

* To whom correspondence should be addressed at the Department of Chemistry, University of California, Berkeley, California 94720.

0022-2364/90 $3.00

erably less than the reduced second-order quadrupole coupling constant (scaled down by the fast inner-rotor spinning); attempts to increase the speed of the outer rotor can lead to a crash of the inner-rotor motion. In order to make DOR more widely applicable, higher spinning speeds could be useful. In addition, synchronization of the outer rotor with the radiofrequency pulses makes it possible to eliminate all the odd-numbered sidebands. In this paper, we describe a new double-rotor design that achieves an outer-rotor speed up to 1 kHz under double-rotation conditions and an associated inner-rotor speed of about 5 kHz. The mechanism leading to the crash of the inner-rotor motion is discussed based on an analysis of the mechanics and experimental data. To demonstrate the performance of this new double rotor, DOR spectra of ^{23}Na and ^{17}O are shown for several situations including sodium oxalate in which the linewidth has been reduced to 80 Hz. Computer simulations of the sideband pattern are shown to be in good agreement with experimentally obtained synchronized spectra.

EXPERIMENTAL

Experiments were carried out on a 400 MHz spectrometer. The static magnetic field was shimmed using the deuterium resonance of D_2O; the linewidth is below 10 Hz in our DOR probe.

Double rotor. A useful double-rotor design must meet, in many aspects, the requirements for a conventional high-performance MAS system. In addition, a further complication with the double rotor arises from the well-known fact that a spinning object, like the inner rotor, has the tendency to maintain its spinning orientation unless a torque is exerted on it. Torque is obviously not desirable here because it imposes an extra burden on the bearing system which only has a limited load capacity. Fortunately, as will be illustrated below, the torque can be reduced to a tolerably small value when the ratio of the angular velocities ω_1/ω_2 approaches a certain fixed value that depends on the structure of the inner rotor.

As illustrated in Fig. 1, the motion of the inner rotor can be visualized as the motion of a rigid cylinder with a fixed point, in this case the cross point of the two rotation axes; the pattern of the motion is the well-known precession motion but without nutation. The equation relevant to such motion is

$$\frac{d\mathbf{J}}{dt} = \tau, \qquad [1]$$

where $\mathbf{J}$ is the angular momentum of the inner rotor and τ is the torque applied to the inner rotor through the bearing. The angular momentum can be expressed in terms of the angular velocity ω as

$$\mathbf{J} = \mathbf{i}I_x\omega_x + \mathbf{j}I_y\omega_y + \mathbf{k}I_z\omega_z, \qquad [2]$$

where $\mathbf{i}$, $\mathbf{j}$, and $\mathbf{k}$ are the unit vectors of the principal axis system (x, y, z) of the moment of inertia tensor of the inner rotor with principal values I_x, I_y, and I_z. In our case, the tensor is symmetric, $I_x = I_y$. There are two contributions to the inner-rotor angular velocity, the angular velocity ω_1 of the inner rotor around its own axis and the angular velocity ω_2 imposed by the outer rotor. This second contribution can be decomposed into two components, $\omega_2\cos\beta_1$ along the z axis, the spinning axis of the

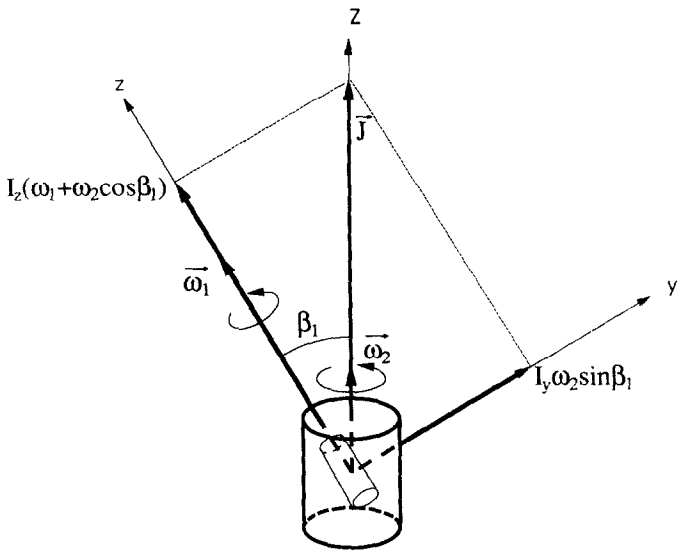

FIG. 1. By adjusting the ratio of moments of inertia (I_y/I_z), the addition of the two vector components of the angular momentum along the inner-rotor axis z and the y axis can be made to point along the outer-rotor axis Z, so that spinning the outer rotor will not affect the orientation of the total angular momentum of the inner rotor.

inner rotor, and $\omega_2 \sin \beta_1$ along the y axis which is chosen to be in the plane of z and Z where the Z direction is along the outer-rotor spinning axis. Thus we have

$$\omega_x = 0, \qquad \omega_y = \omega_2 \sin \beta_1, \qquad \omega_z = \omega_1 + \omega_2 \cos \beta_1. \tag{3}$$

Viewed from the laboratory frame, the only way to make **J** time-independent, with no torque, is to design the system in such a way that **J** points along the Z axis as depicted in Fig. 1, i.e.,

$$\tan \beta_1 = \frac{I_y \omega_2 \sin \beta_1}{I_z(\omega_1 + \omega_2 \cos \beta_1)} \tag{4}$$

or

$$\omega_1/\omega_2 = \cos \beta_1 \left(\frac{I_y}{I_z} - 1 \right) \equiv k. \tag{5}$$

Clearly, for a fixed ratio of I_y/I_z, determined by the dimensions of the inner rotor, the ratio ω_1/ω_2 is fixed for the torque-free condition.

For a ratio ω_1/ω_2 of 5, when the outer-rotor speed reaches 1 kHz, the inner-rotor speed must be 5 kHz, which is not difficult to achieve with current techniques. Since the inner rotor is inclined at an angle inside the outer rotor, the dimensions of the inner rotor (both the length and the diameter) will determine the eventual diameter of the outer rotor which is a crucial factor in obtaining high outer-rotor speeds. With the goal of producing higher speeds for both the inner and outer rotors, we have

designed a new double rotor with a reduced diameter of the outer rotor and a turbine system for the inner rotor with parameters recommended for MAS operation (*5*); the driving jets are placed at both ends of the inner rotor.

An illustrative sketch of the double-rotor probe is shown in Fig. 2. For the purpose of detailed studies of the inner-rotor behavior, we used a two-port air injection system similar to the original design (*4*) as shown in detail in Fig. 2a. In principle, one-port air injection is sufficient and stable if the position of the outer rotor is fixed with a flat air bearing from the bottom as shown in Fig. 2b. The new double rotor, as shown in Fig. 2c, is machined in three pieces held together with the axle (part 13) and the step shoulders (part 14) on the center piece (part 2) by press-fitting into the matched counter parts (parts 13′ and 14′) on the end pieces (part 2′). This structure has several advantages. The cylindrical structure of the center piece allows efficient use of the available space within the outer rotor. Moreover, the cylindrical shape also prevents structural deformations; deviations less than 0.015 mm can be made over the whole length of the outer rotor. In addition, we can use more fragile ceramic materials for the rotor body because a tight press fit of the matching pieces is not necessary here; we can use clamp buttons screwed on top of the axles (part 13) to hold the three pieces together as well. The new structure also prevents any air leakage through mismatched fits. As a result of these modifications and of reducing the inner-rotor diameter to 4.6 mm, we were able to reduce the outer rotor diameter to 13 mm, with a length of 46 mm. A further reduction of length and diameter is possible with a one-port air injection system feeding both the bearing and the drive of the inner rotor as shown in Fig. 2b. The outer rotor described above is able to reach an angular velocity of 2 kHz after careful balancing under conditions of single rotation; a spinning inner rotor has no appreciable influence on the outer-rotor performance when the outer rotor is spinning below 1 kHz.

To operate the double rotor, we first spin the inner rotor and then the outer rotor. Initially, the ratio ω_1/ω_2 is too high to satisfy the torque-free condition discussed above. Consequently, a torque is generated, and the increased friction on the inner rotor from the bearing system slows down spinning of the inner rotor; at the same time, the ratio ω_1/ω_2 decreases and with it the torque and friction, finally stabilizing the inner-rotor spinning speed at a lower value close to the torque-free condition. As the outer-rotor speed increases, the inner-rotor speed also increases automatically in order to adapt itself to the torque-free condition. In fact, precisely at the torque-free condition the system is not stable, since any accidental slow-down of the inner rotor can trigger a torque avalanche. To be more specific, any decrease of ω_1 increases the

FIG. 2. New double-rotor probe designs. (a) Double-rotor probe with two-port air injection. (b) Double-rotor probe with one-port air injection. (c) Details of new double rotor. (1) inner rotor with flutes at both ends; (2 and 2′) building blocks of the double rotor held together through the axles (13) with the matched counter parts (13′), and the step shoulder (14) with the matched counter parts (14′); (3 and 4) air channels and holes for bearing and drive system of the inner-rotor; (5) pins to hold the inner-rotor in place; (6 and 7) bearing and drive system for the outer-rotor; (8) air exhaust holes for the outer rotor; (9) pins to hold the outer-rotor in place; (10) air passage for the inner rotor which fits into (10′) with small clearance; (11) space for RF coil; (12) bearing system on which the outer rotor floats; (15) caps holding inner rotor in place and allowing air escape for the inner-rotor system.

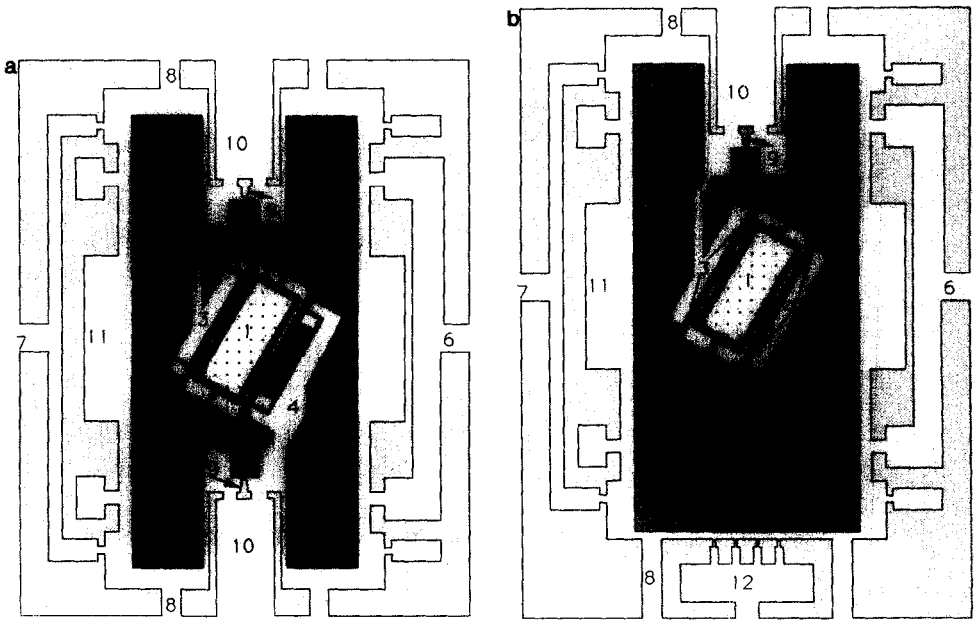
a
8
10
11
7
6
10
8
b
8
10
11
7
6
8
12

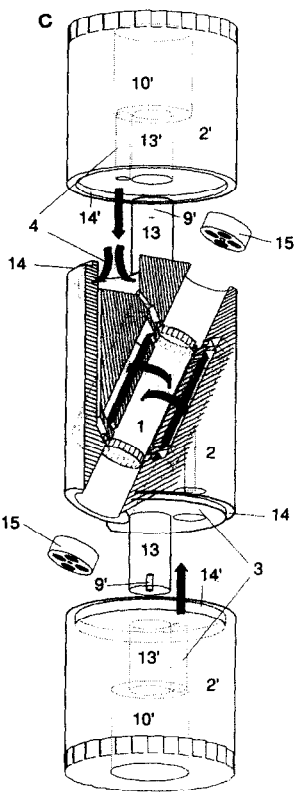
c
10'
13'
2'
4
14'
9'
13
15
14
1
2
14
15
13
9'
14'
3
13'
2'
10'

torque when the ratio ω_1/ω_2 is at the torque-free condition; this in turn decreases ω_1 implying a further increase of the torque and leading finally to a crash of the inner-rotor motion; the outer-rotor system is too large for ω_2 to adapt itself quickly to any change of the inner-rotor motion. On the contrary, the system is in a stable state when the ratio ω_1/ω_2 is close, but higher than the torque-free condition, as long as the weak torque generated can be tolerated by the bearing system of the inner rotor. Any accidental slow-down of the inner rotor will now decrease the torque and friction, bringing ω_1 up again; similarly, any accidental speed-up of the inner rotor will increase the torque bringing ω_1 down again. This self-adjusting mechanism protects the inner rotor against any instabilities. It can be shown (*6*) that under the influence of a torque the relationship between ω_1 and ω_2 can be written as

$$\omega_1 = \cos\beta_1(I_y/I_z - 1)\omega_2 + \frac{\tau}{I_z\omega_2 \sin\beta_1} \equiv k\omega_2 + \Delta\omega_1 \qquad [6]$$

which reduces to Eq. [5], the torque-free condition, when τ (the absolute magnitude of τ in Eq. [1]) or $\Delta\omega_1$ is set to zero.

Both the inner- and outer-rotor spinning speeds can be measured experimentally from the sideband positions of ^{23}Na in sodium chloride where the line is broadened by dipole–dipole interactions. The sidebands resulting from motions of the inner and the outer rotors can be clearly distinguished owing to the large ω_1/ω_2 ratio which effectively adiabatically decouples the NMR effects of the two rotors. Figure 3 shows an example of such a spectrum; sidebands due to the inner rotor can be clearly seen from the magnified spectrum. Figure 4 is a plot of $\nu_1 = \omega_1/2\pi$ versus $\nu_2 = \omega_2/2\pi$ obtained for two different inner rotors; A is 13.3 mm long and B is 15.2 mm long with k values of 4.5 and 5.1, respectively. The different specific gravities of Vespel and sodium chloride have been taken into account in the calculation of k. Points in Fig. 4 represented by same solid symbols are obtained under the same conditions for the inner rotor, i.e., the same bearing and drive air pressures. The plot shows that the inner-rotor speed depends linearly on the outer-rotor speed over a wide range of ν_2, but tends to deviate from it when ν_2 comes closer to the point where the motion of the inner rotor crashes. The experimental slope k obtained from the linear fitting is 4.9 for rotor A and is 5.4 for rotor B and does not depend on the air pressure used; moreover, these values are quite close to the calculated values. According to Eq. [6], this implies that the torque exerted on the inner rotor through the bearing adjusts itself with ω_2 until it can no longer be tolerated by the bearing system. The intercept of ν_1 at $\nu_2 = 0$ is not zero and is larger for rotor B which makes the deviation from the linearity more significant when $\Delta\nu_1 = \Delta\omega_1/2\pi$ starts to change. The nonzero positive value of $\Delta\nu_1$ is in agreement with our argument above based on the stability argument requiring that ν_1 must slightly exceed the value dictated by the torque-free condition. The relationship between $\Delta\nu_1$ and the air pressure used to operate the inner rotor depends on the details of the inner-rotor bearing and drive system; as seen in Fig. 4, the inner rotor A has a smaller $\Delta\nu_1$ value than B for the same air pressure and it depends less sensitively on the air pressure used.

Synchronization. There are three different axes in the DOR experiment, namely the static magnetic field, the inner-rotor axis, and the outer-rotor axis. The relative positions of these three axes at the time when the RF pulse is applied is important for

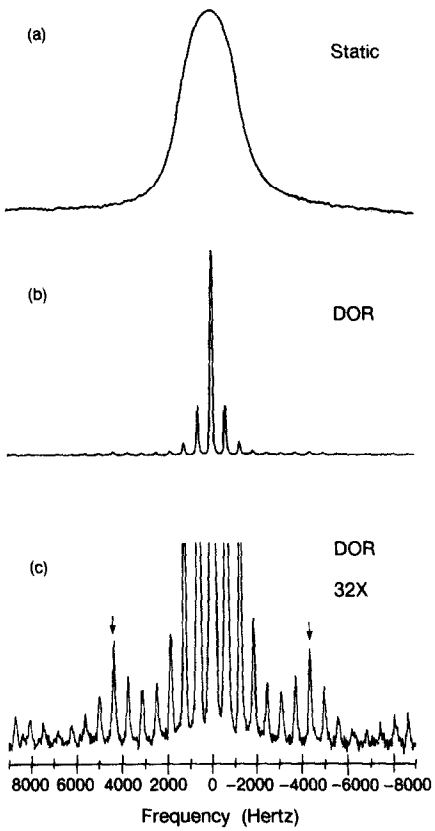

FIG. 3. (a) Static spectrum of ^{23}Na in polycrystalline NaCl. (b) DOR spectrum obtained with ν_1 = 4.4 kHz and ν_2 = 620 Hz. The sidebands seen in this spectrum arise from spinning of the outer rotor. By expanding this spectrum 32 times (c), the sidebands corresponding to spinning of the inner rotor can be recognized and are indicated by the arrows.

the evolution of the spin system (*7*). When the three axes are coplanar, two angles can be defined, namely, $\gamma_1 = 0°$ when the outer-rotor axis is between the magnetic field orientation and the inner-rotor axis and $\gamma_1 = 180°$ when the inner-rotor axis is between the magnetic field and the outer-rotor axis. By synchronizing the RF pulse with the rotor motion alternately at $\gamma_1 = 0°$ and $\gamma_1 = 180°$ and adding the two spectra together, odd-numbered sidebands can be eliminated.

Synchronization is realized with a homemade apparatus consisting of two parts, a light sensor and a logic circuit. Two light-reflecting white marks painted on the external surface of the outer rotor and separated by 180° are detected by light reflected from an optical fiber. When the outer rotor spins, the two white marks pass through the light beam sending out TTL pulses to the logic circuit. The logic circuit splits the train of TTL pulses from the light sensor alternately into two output channels so that each channel contains TTL pulses corresponding only to one of the two white marks. The acquisition event is triggered externally by TTL pulses which, in our case, come from

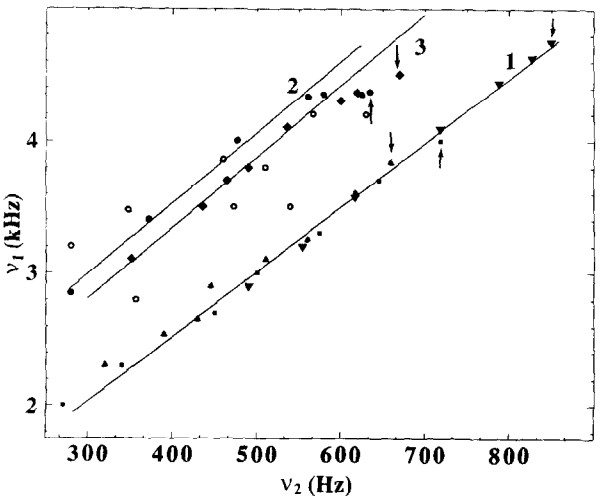

FIG. 4. The inner-rotor spinning speed ν_1 is plotted versus the outer-rotor spinning speed ν_2. The symbols ▲, ■, and ▼ represent data for inner rotor A (see text) obtained with air pressures of 25, 30, and 35 psi, respectively. Line 1 is a linear fit for all of these data with $k = 4.9$ and $\Delta\nu_1 = 573$ Hz (see Eq. [6]). The arrows indicate the highest ν_2 speeds before the motion of the inner rotor crashes. The symbols ○, ●, and ◆ represent data for inner rotor B (see text) for which ● were obtained with an air pressure of 30 psi and ◆ with an air pressure of 35 psi; ○ were obtained with variable air pressures. Line 2 is a linear fitting for ● with $k = 5.3$ and $\Delta\nu_1 = 1.4$ kHz; line 3 is a linear fit for ◆ with $k = 5.4$ and $\Delta\nu_1 = 1.2$ kHz.

one of the output channels of the logic circuit. The output of the logic circuit can toggle between the two output channels whenever it receives an external TTL pulse; this external TTL pulse is transmitted from the spectrometer interface after each acquisition event. In this way, the acquisition is triggered alternately by TTL pulses corresponding to the two white marks. By inserting a proper delay time between the external trigger and acquisition, the acquisition can be set exactly at $\gamma_1 = 0°$ and $\gamma_1 = 180°$.

RESULTS

To show the effect of the outer-rotor speed on the sideband pattern in the case of quadrupole interactions, the central transition spectra of ^{23}Na in sodium oxalate are presented in Fig. 5. Figure 5a shows the static powder pattern which arises from the second-order anisotropic broadening of the quadrupole interaction, the chemical-shift anisotropy, and the dipole–dipole couplings. The linewidth is about 10 kHz. When the sample is subjected to a slow double rotation at $\nu_2 = 200$ Hz (Fig. 5b), sharp peaks start to appear; the overall lineshape becomes a superposition of sidebands separated from each other by ν_2. As ν_2 increases to 320 Hz (Fig. 5c), all the sidebands separate and the linewidth decreases to 110 Hz. The centerband is hardly recognizable in this spectrum. At $\nu_2 = 440$ Hz (Fig. 5d), the centerband starts to emerge above all the sidebands and the linewidth decreases further to 100 Hz. When ν_2 goes up through 640 Hz (Fig. 5e) to 850 Hz (Fig. 5f), the linewidth narrows down to 85 Hz. The

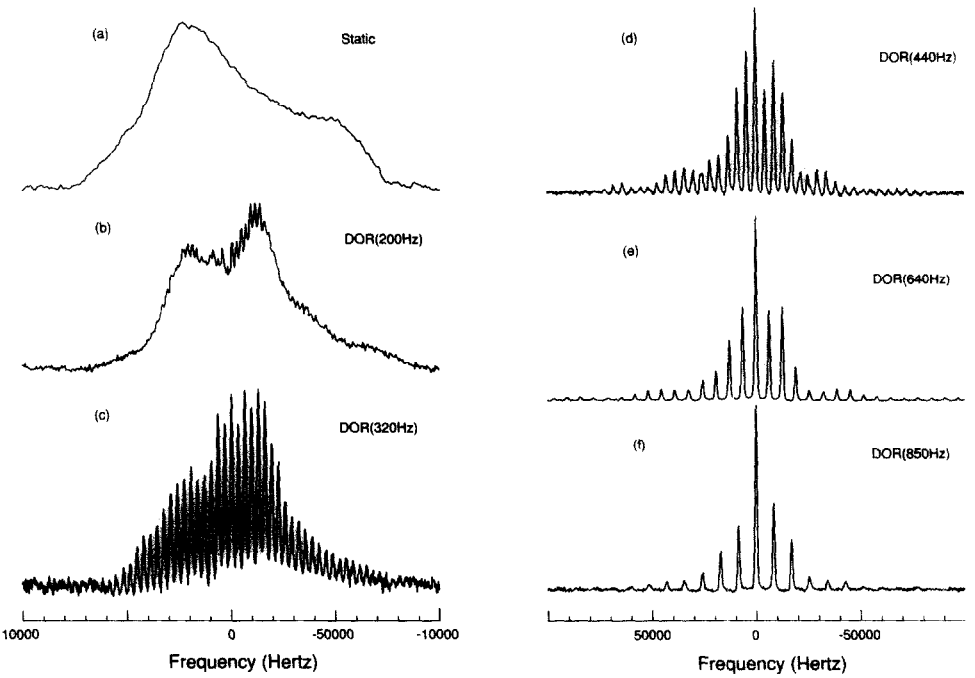

FIG. 5. NMR spectra of ^{23}Na central transition in polycrystalline sodium oxalate. (a) is the static spectrum which has a linewidth about 10 kHz. (b), (c), (d), (e), and (f) are DOR spectra with ν_2 (the angular velocity of the outer rotor) as indicated.

residual linewidth thus depends on rotation speed[1] and arises primarily from dipole–dipole interactions among the ^{23}Na spins. This is because the dipole–dipole interactions cannot be fully truncated by the inner-rotor rotation if the dipole–dipole coupling constants ω_D are not negligibly small compared with the inner-rotor speed ω_1. Contributions of higher-order quadrupole interactions are negligible since the third-order contribution vanishes. Other possible contributions to the linewidth are the inhomogeneity of the magnetic field, defects in the crystalline structure, and errors of the magic-angle setting. The spectra in Fig. 5 are obtained without synchronization. The sideband pattern is an average over a random set of γ_1 values.

Figure 6 shows the unsynchronized spectra and the corresponding synchronized spectra for two different outer-rotor speeds, 604 Hz and 800 Hz. Both of the synchronized spectra are obtained with 10 scans and, indeed, addition of the spectra obtained at $\gamma_1 = 0°$ and $\gamma_1 = 180°$ eliminates the odd-numbered sidebands. The sideband pattern can be simulated (since the parameter γ_1 is known) using values of $(e^2qQ/h) = 2.43 \pm 0.02$ MHz and $\eta = 0.77 \pm 0.02$. In general, however, the DOR sideband pattern contains both first- and second-order effects, i.e., the effects of not only quadrupole interactions, but also chemical shifts and other interactions. The centerband

[1] The linewidth depends mainly on the inner-rotor speed in this case. The outer-rotor speed indirectly affects the linewidth through its influence on the inner-rotor speed as discussed in the text.

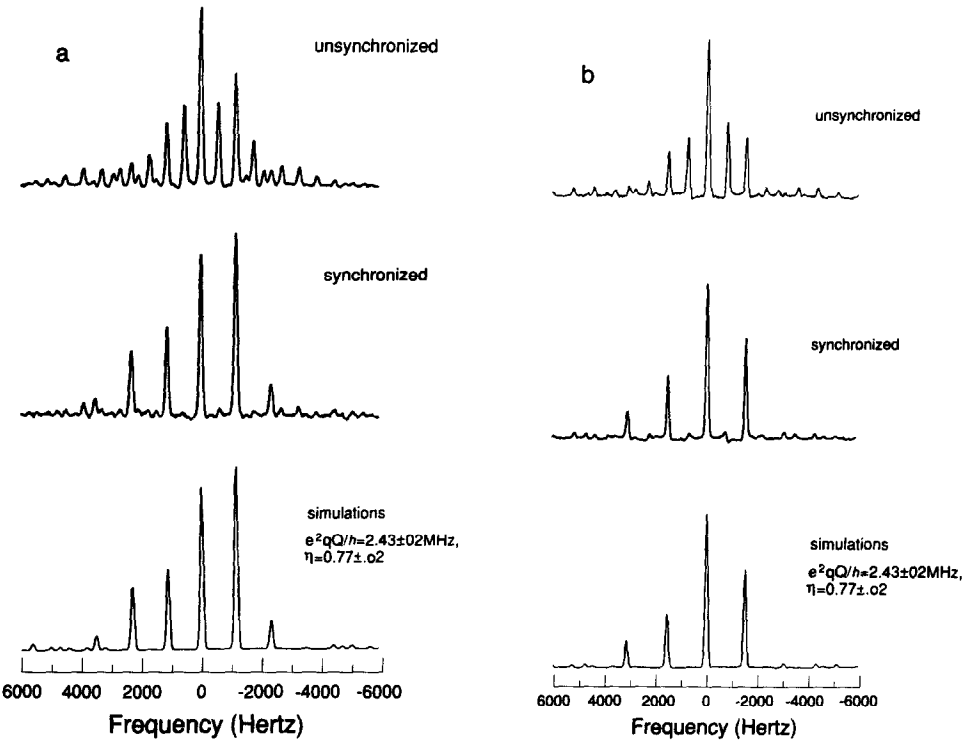

FIG. 6. The effects of synchronizing the outer rotor at angles $\gamma = 0°$ and 180° with RF pulses on the DOR spectra of ^{23}Na in polycrystalline sodium oxalate. (a) shows the unsynchronized and the synchronized spectra at $\nu_2 = 604$ Hz. A computer simulation is also shown with $(e^2qQ/h) = 2.43$ MHz and $\eta = 0.77$. (b) shows similar spectra obtained with $\nu_2 = 800$ Hz. The computer simulation uses the same parameters as in (a).

lineshape in MAS does not contain information about first-order effects (except for homogeneous interactions which are negligible in high-speed MAS compared with the second-order quadrupole interaction).

Figure 7 shows ^{23}Na spectra of a sample containing a mixture of sodium sulfate and sodium oxalate of which the molar ratio of sodium atoms is 2:1. The static spectrum shown in Fig. 7a is again 10 kHz wide. Under MAS at 5.7 kHz (Fig. 7b), the linewidth is reduced to 2.5 kHz and some structure is visible. Under DOR (Fig. 7c), the line collapses into sharp lines and the two-peak structure is clearly revealed; the intensity ratio of the two components is 2:1 just as expected and the linewidth is 80 Hz (0.8 ppm) for both lines.

Finally, we demonstrate the resolution of this DOR probe with ^{17}O spectra of a sample of the mineral wollastonite which contains nine crystographically distinct oxygen sites. Figures 8a and 8b show the static and MAS spectra. Higher MAS spinning speeds do not help to improve the resolution since the spectrum is broadened mainly by quadrupole interactions. The resolution is improved by DOR as shown in Fig. 8c. Eight different lines can be identified and are indicated by arrows. The linewidth is about 70 Hz (0.7 ppm). Those peaks not indicated by arrows are spinning sidebands

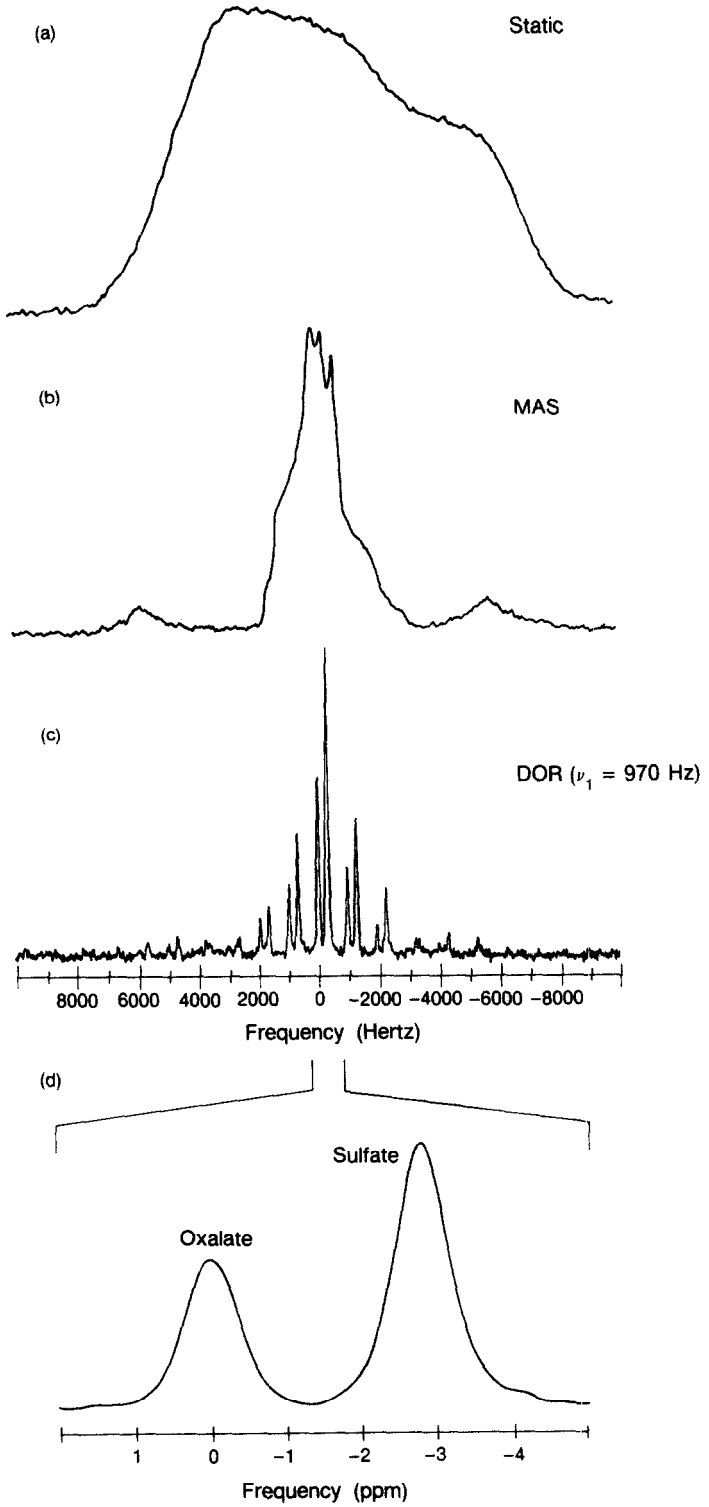

FIG. 7. NMR spectra of ^{23}Na central transition in a 2:1 polycrystalline mixture of sodium sulfate and sodium oxalate. (a) is the static spectrum and (b) is the MAS spectrum with rotor spinning speed of 5.7 kHz. (c) is the DOR spectrum with ν_2 = 970 Hz clearly revealing the two line structure. (d) is an expanded version of (c) showing the centerband peaks originating from the two components of the mixture.

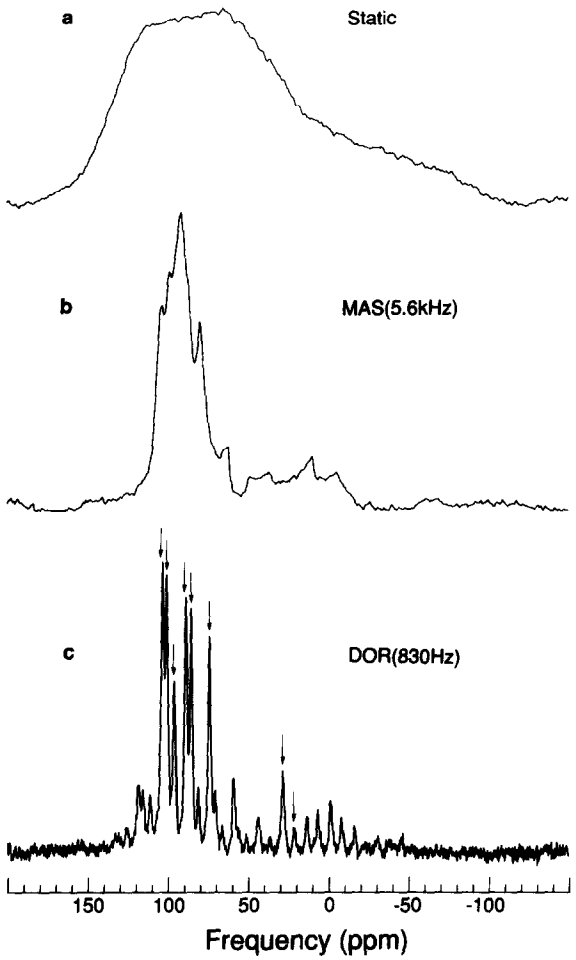

FIG. 8. NMR spectra of ^{17}O central transition in polycrystalline ($CaSiO_3$) wollastonite. (a) Static spectrum; (b) MAS spectrum with a rotor speed of 5.6 kHz; (c) DOR spectrum with ν_2 = 830 Hz. Lines arising from eight resolved oxygen sites are indicated by arrows. The chemical-shift reference is ^{17}O in water.

associated with the spinning of the outer rotor identified by using different outer-rotor speeds.

CONCLUSIONS

A new double-rotor design achieves an outer-rotor speed of about 1 kHz and an inner-rotor speed of 5 kHz under DOR conditions. Based on a simple model, the mechanics of the double rotor can be understood and verified experimentally by measuring the spinning speeds of both the inner and the outer rotors. The important point is that the torque-free condition is not a stable state and a certain amount of excess speed is needed for the inner rotor in order to maintain a stable motion. The excess speed depends on various quantities such as the torque, the moment of inertia, and the outer-rotor speed. The mechanism causing the inner rotor to crash and ideas on

how to improve the double-rotor performance are now clearer. Further improvement and other designs are under way in our laboratory.

The outer-rotor speed influences the sideband pattern for the case of quadrupole interactions and being able to spin at higher speeds improves the resolution of the centerband and reduces the sidebands significantly. With synchronization, the odd-numbered sidebands are completely eliminated and the sideband pattern can be simulated rapidly and accurately due to the known geometric relationship between the two rotation axes and the magnetic field orientation. Experimental spectra on ^{23}Na in sodium chloride, sodium oxalate, and sodium sulfate and on ^{17}O in wollastonite illustrate the performance of the double rotor.

ACKNOWLEDGMENTS

We are grateful to B. F. Chmelka and J. Stebbins for the ^{17}O-enriched wollastonite sample, to G. C. Chingas and Z-y. Peng for help in the design of the synchronization apparatus, and to C. Gaskins for machining parts for the new double rotor. This work was supported by the Director, Office of Energy Research, Office of Basic Energy Sciences, Materials Sciences Division of the U.S. Department of Energy under Contract DE-AC03-76SF00098.

REFERENCES

1. E. R. ANDREW, A. BRADBURY, AND R. G. EADES, *Arch. Sci.* **11,** 223 (1958); I. J. LOWE, *Phys. Rev. Lett.*, **2,** 285 (1959).
2. A. BAX, N. M. SZEVERENYI, AND G. E. MACIEL, *J. Magn. Reson.* **52,** 147 (1983); A. BAX, N. M. SZEVERENYI, AND G. E. MACIEL, *J. Magn. Reson.* **55,** 494 (1983); T. TERAO, H. MIURA, AND A. SAIKA, *J. Chem. Phys.* **85,** 3816 (1986).
3. A. LLOR AND J. VIRLET, *Chem. Phys. Lett.* **152,** 248 (1988); A. SAMOSON, E. LIPPMAA, AND A. PINES, *Mol. Phys.* **65,** 1013 (1988); B. F. CHMELKA, K. T. MUELLER, A. PINES, J. STEBBINS, Y. WU, AND J. W. ZWANZIGER, *Nature (London)* **339,** 42 (1989); K. T. MUELLER, B. Q. SUN, G. C. CHINGAS, AND J. W. ZWANZIGER, *J. Magn. Reson.* **86,** 470 (1990).
4. A. SAMOSON AND A. PINES, *Rev. Sci. Instrum.* **60,** 3239 (1989).
5. F. D. DOTY AND P. D. ELLIS, *Rev. Sci. Instrum.* **52,** 1868 (1981).
6. R. J. STEPHENSON, "Mechanics and Properties of Matter," Wiley, New York, 1969.
7. A. SAMOSON AND E. LIPPMAA, *J. Magn. Reson.* **84,** 410 (1989).